nature physics

SUPPLEMENTARY INFORMATION

DOI: 10.1038/NPHYS3962

In the format provided by the authors and unedited.

A global inversion-symmetry-broken phase inside the pseudogap region of $YBa_2Cu_3O_y$

Contents:

S1. Simulated RA patterns for the orthorhombic *mmm* point group

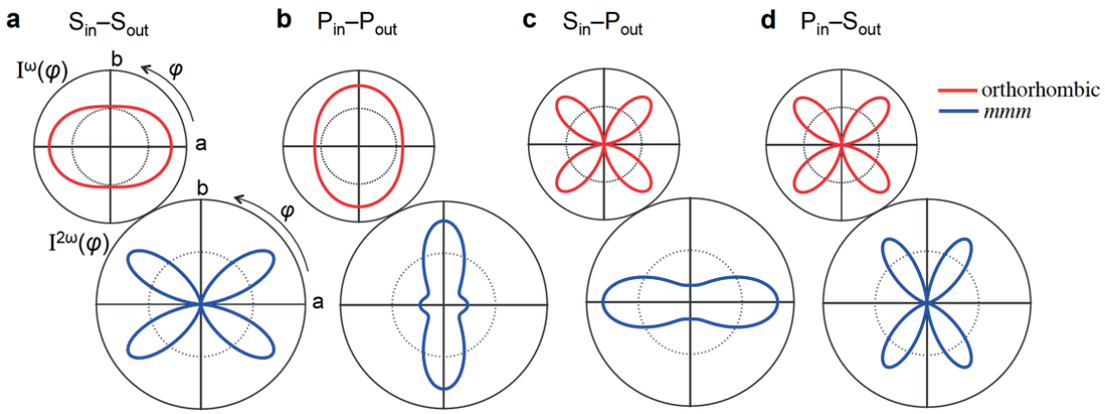

Fig. S1. Simulated linear and SH RA patterns for hole-doped $YBa_2Cu_3O_y$ using an orthorhombic crystal class and *mmm* point group respectively for all four polarization geometries **a**, S_{in}–S_{out} (reproduced from Fig. 1b of the main text), **b**, P_{in}–P_{out}, **c**, S_{in}–P_{out} and **d**, P_{in}–S_{out}.

We computed linear and SH RA patterns in the electric-dipole and electric-quadrupole approximations for an orthorhombic crystal system and *mmm* point group respectively. The mathematical expressions for $I^{\omega}(\varphi)$ and $I^{2\omega}(\varphi)$ are given in the Methods section. In the orthorhombic crystal class χ_{ij}^{ED} has 3 non-zero independent elements (*xx, yy, zz*). In the *mmm* point group and degenerate SH configuration χ_{ijkl}^{EQ} has 15 non-zero independent elements (*xxxx, xxyy = xyyx, xxzz = xzzx, xyxy, xzxz, yxxy = yyxx, yxyx, yyyy, yyzz = yzzy, yzyz, zxzx, zyzy, zzxx = zxxz, zzyy = zyyz, zzzz*). Figure S1 shows the representative RA patterns computed under all four possible polarization geometries. The P_{in}–P_{out}, S_{in}–P_{out} and P_{in}–S_{out} simulations reproduce all of the symmetries of the S_{in}–S_{out} data shown in Fig. 1b of the main text (Fig. S1a) as expected.

S2. RA data for P_{in}-P_{out}, S_{in}-P_{out} and P_{in}-S_{out} geometries above T_Ω

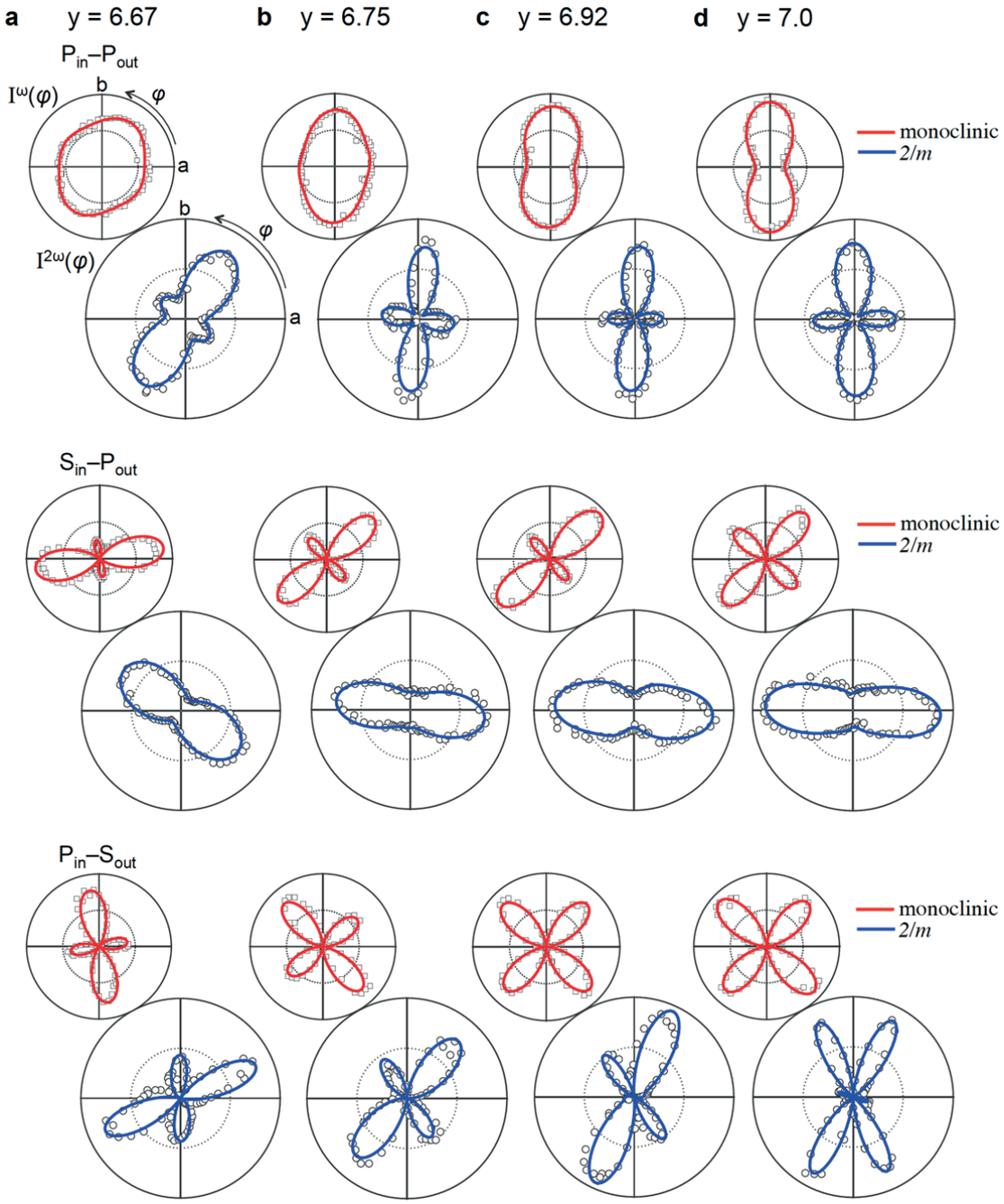

Fig. S2. Linear and SH RA data on hole-doped $YBa_2Cu_3O_y$ with **a**, y = 6.67, **b**, y = 6.75, **c**, y = 6.92 and **d**, y = 7.0 in P_{in}–P_{out} (first row), S_{in}–P_{out} (second row), and P_{in}–S_{out} (third row) geometries taken at room temperature. Fits to an electric-dipole induced linear response from a monoclinic crystal system (red curves) and to an electric-quadrupole induced SH response from a 2/*m* point group (blue curves) are overlaid.

Figure S2 shows linear and SH RA data acquired from the four hole-doping levels of $YBa_2Cu_3O_y$ used in this study under P_{in}–P_{out}, S_{in}–P_{out} and P_{in}–S_{out} polarization geometries at room temperature. These data violate the symmetries of the orthorhombic crystal class and *mmm* point group in a manner consistent with the S_{in}–S_{out} data shown in Fig. 2 of the main text. Using the same mathematical expressions for $I^{\omega}(\varphi)$ and $I^{2\omega}(\varphi)$ as those used to fit the S_{in}–S_{out} data shown in Fig. 2 of the main text (see Methods), excellent fits to the data for all doping levels and polarization geometries were obtained (Fig. S2), thus further confirming our monoclinic 2/*m* point group assignment. Figure S2 also shows that the degree of monoclinicity decreases monotonically between $y = 6.67$ and $y = 7$ for all polarization geometries, which corroborates the S_{in}–S_{out} data shown in Fig. 2 of the main text.

S3. Fits of SH RA data above T_Ω to other monoclinic point groups and radiation sources

i. Electric-dipole induced SH from the 2 point group

By applying C_2 symmetry and the degenerate SH permutation symmetries alone, χ_{ijk}^{ED} is reduced to 8 non-zero independent elements (*xxz = xzx, xyz = xzy, yxz = yzx, yyz = yzy, zxx, zxy = zyx, zyy, zzz*), which yields zero response in the S_{in}–S_{out} polarization geometry. By extension, any non-centrosymmetric point group that includes C_2 as a symmetry element cannot generate an electric-dipole induced SH response in S_{in}–S_{out} polarization geometry. Therefore the data shown in Fig. 2 and Fig. 4 of the main text, which have finite S_{in}–S_{out} signals, cannot be explained by any non-centrosymmetric point group that contains C_2.

ii. Electric-dipole induced SH from the m point group

The m point group explicitly violates C_2, which is present in all of the room temperature data shown in Fig. 2 of the main text and in Fig. S2. Therefore it is ruled out.

iii. Magnetic-dipole induced SH from the $2/m$ point group

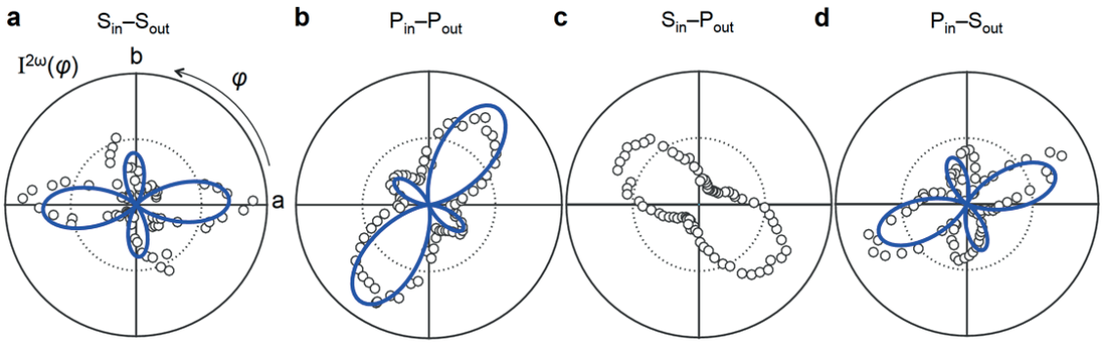

Fig. S3. SH RA data from $YBa_2Cu_3O_{6.67}$ taken in **a**, S_{in}–S_{out}, **b**, P_{in}–P_{out}, **c**, S_{in}–P_{out}, and **d**, P_{in}–S_{out} geometry at room temperature. Blue curves are fits to the bulk magnetic-dipole SH contribution under point group *2/m*.

Magnetic-dipole induced SH is described by the process $M_i^{2\omega} \propto \chi_{ijk}^{MD} E_j^{\omega} E_k^{\omega}$ where M is the induced magnetization and E is the incident electric field. The axial rank-3 magnetic-dipole susceptibility tensor χ_{ijk}^{MD} is allowed in centrosymmetric crystals. By applying the 2/*m* point

group symmetries and degenerate SH permutation symmetries, χ_{ijk}^{MD} is reduced to 8 non-zero independent elements (*xxz = xzx, xyz = xzy, yxz = yzx, yyz = yzy, zxx, zxy = zyx, zyy, zzz*), which yields zero response in the S_{in}–P_{out} polarization geometry. This clearly disagrees with the data shown in Fig. S2. Moreover, a best fit to other polarization geometries does not provide good agreement (Fig. S3). Therefore the magnetic-dipole response is ruled out.

iv. Surface electric-dipole induced SH from the $2/m$ point group

The surface of any crystal necessarily breaks inversion symmetry and will allow electric-dipole SH generation. However, the (001) surface of a bulk 2/*m* point group contains C_2 and therefore yields zero response in S_{in}–S_{out} polarization geometry based on the arguments presented in sub-section (i). Therefore the SH response observed above T_Ω must originate from a source other than the surface electric-dipole contribution.

We note that the additional SH intensity observed below T_Ω (Figs 3 & 4 of main text) also cannot originate from the surface. First, the temperature at which this symmetry breaking occurs coincides with the known bulk *T** value for all different doping levels studied. Second, if the enhancement of SH intensity observed below *T** did in fact originate from the surface, it would imply a corresponding enhancement of the surface electric-dipole radiation efficiency at 1.5 eV incident energy. However the bulk sensitive linear optical response, which is likewise sensitive to electric-dipole transitions at 1.5 eV, shows no detectable change across *T** (Fig. 3 main text). The only way to reconcile these statements is if a significant change in electric-dipole transition rates at 1.5 eV happened to take place exclusively at the surface across the bulk *T** value, which to our knowledge has no experimental or theoretical precedent. Therefore we rule out this scenario.

S4. Temperature dependence of SH RA data above T_Ω

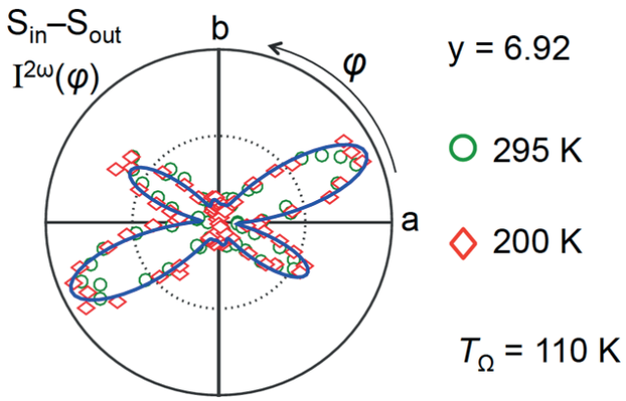

Fig. S4. SH RA data from $YBa_2Cu_3O_{6.92}$ acquired in S_{in}–S_{out} polarization geometry at temperatures $T = 295$ K (green circles) and $T = 200$ K (red diamonds), which are both well above $T_\Omega \sim 110$ K. The blue curve is a best fit to the $T = 295$ K data assuming electric-quadrupole induced SH from a 2/*m* point group.

To search for changes in crystallographic structure at temperatures above T_Ω, we performed SH RA measurements as a function of temperature for $T > T_\Omega$. No changes in both intensity and pattern shape were detected above T_Ω across all four doping levels and polarization geometries. Figure S4 shows representative SH RA patterns from $YBa_2Cu_3O_{6.92}$ in S_{in}–S_{out} geometry acquired at $T = 200$ K and $T = 295$ K, which are both well above its measured value of $T_\Omega \sim 110$ K and are nearly identical. This shows that the monoclinic distortion of the lattice sets in above room temperature.

S5. SH RA patterns above and below T_Ω for all doping levels

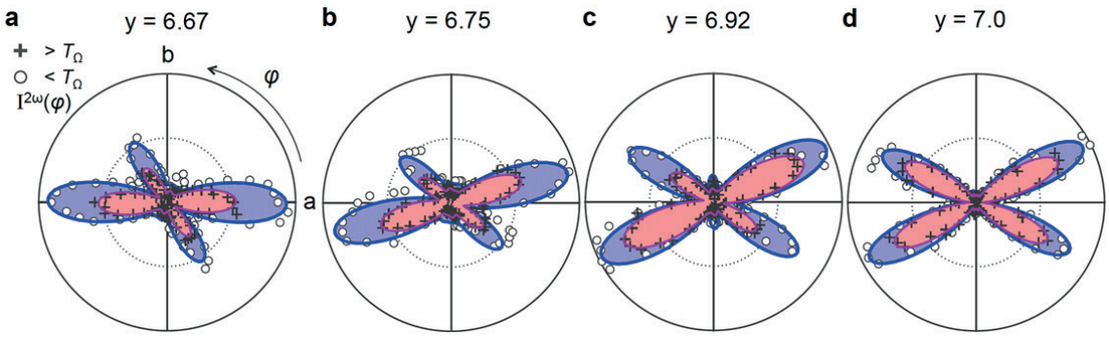

Fig. S5. SH RA data from hole-doped $YBa_2Cu_3O_y$ taken in S_{in}–S_{out} polarization geometry both above (crosses) and below (circles) T_Ω. The high temperature data were all acquired at $T = 295$ K while the low temperature data were acquired at **a**, $T = 80$ K for y = 6.67, **b**, $T = 80$ K for y = 6.75, **c**, $T = 30$ K for y = 6.92 and **d**, $T = 15$ K for y = 7.0. Red and blue shaded regions are the best fits to the high and low temperature data respectively using the same models as those described in Fig. 4 of the main text.

Figure S5 shows the SH RA patterns taken both above and below T_Ω for the complete set of doping levels in S_{in}–S_{out} polarization geometry. For all doping levels, the intensity is enhanced below T_Ω consistent with Fig. 3 of the main text and fit excellently to the same two domain model applied to the data shown in Fig. 4 of the main text.

S6. List of subgroups of 2/*m*

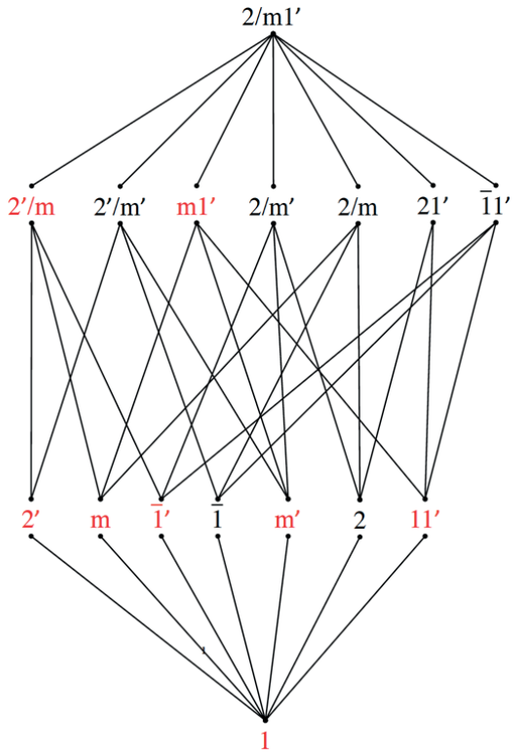

Fig. S6. Tree diagram showing all magnetic and non-magnetic subgroups of the 2/*m* point group (re-written as 2/*m*1′). Lines connect parent groups to their subgroups. The non-centrosymmetric subgroups that do not contain C_2 are shown in red.

The complete set of magnetic and non-magnetic subgroups of the crystallographic monoclinic point group 2/*m* is displayed in Fig. S6. The point group 2/*m* is re-written as 2/*m*1′ to make the relationship to its magnetic subgroups more obvious. The generators are defined as follows: 2 → 180° rotation about the *c*-axis, *m* → reflection about *ab*-plane, 1 → identity, $\bar{1}$ → spatial inversion, *A*′ → combination of any spatial operation *A* with time-reversal. There are a total of 15 subgroups of 2/*m*1′ (excluding 2/*m*1′ itself) of which the 8 shown in red are non-centrosymmetric and do not contain C_2. The 2′/*m* and *m*1′ subgroups are independent (i.e. one is not a subgroup of the other) and contain all of the other 6 red subgroups.

S7. Exclusion of laser-induced changes to the samples

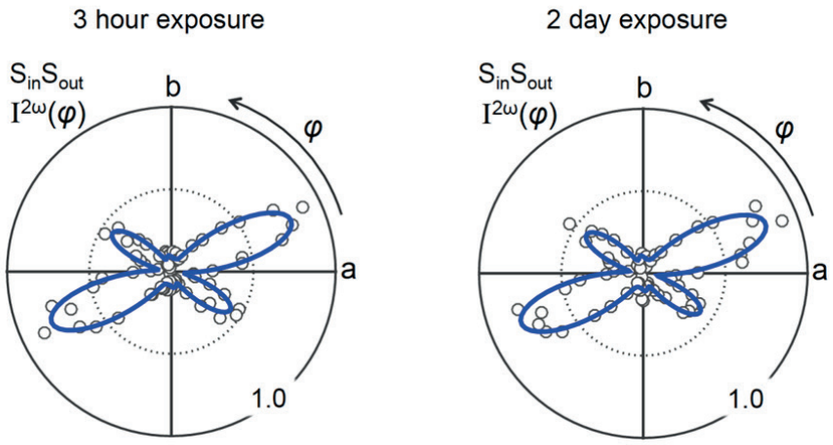

Fig. S7. SH RA data from optimal doped $YBa_2Cu_3O_{6.92}$ taken in S_{in}–S_{out} polarization geometry at $T = 295$ K following a 3 hour and 2 day exposure to laser light. Blue curves are fits as described in the main text.

To verify that the laser beam is not inducing any change in the samples, particularly not creating additional oxygen vacancies, we performed SH RA measurements following different laser exposure times. Knowing that the SH RA patterns are highly sensitive to oxygen content (Fig. 2 main text), if the laser were inducing additional oxygen vacancies, one would expect the SH RA patterns to evolve towards those associated with lower oxygen content upon increased laser exposure time. However, we do not observe any obvious change in the SH RA pattern as a function of continuous laser exposure time for any of the samples studied. To give an example, Fig. S7 shows a comparison of two room temperature SH RA patterns measured from the same spot on an optimal doped sample (y = 6.92) after 3 hours versus 2 days of laser exposure plotted on the same intensity scale, which show no measurable difference. [Note: 3 hours is the typical time we require to align the sample]. Moreover, for all doping levels studied, the onset temperatures T_Ω of the symmetry breaking coincide with the known values of T^* (Fig. 3e main text). Therefore, we rule out any laser-induced changes to the samples.

S8. Exclusion of misalignment as origin of RA patterns

We can rule out misalignment of any form as the origin of the observed RA patterns for the following independent set of reasons:

1) The flat as-grown faces of the crystals are extremely well aligned perpendicular to the *c*-axis. We know this because atomic force microscopy performed on as-grown crystals show very large micron sized terraces separated by unit-cell tall steps. Therefore any angular misalignment between the surface normal and the *c*-axis would not exceed approximately 1 nm (step height) / 1000 nm (terrace length) = 0.001 radians ≈ 0.06°.

The experimental optical axis is also extremely well aligned perpendicular to the crystal surface. This alignment is performed by ensuring overlap between a collimated incident beam and the retro-reflected beam over a distance of 1 m. Therefore any angular misalignment between the optical axis and the surface normal would not exceed approximately 1 mm (collimated beam diameter) / 1000 mm (beam overlap distance) = 0.001 radians ≈ 0.06°.

The two facts above together demonstrate that the experimental optical axis is extremely well aligned to the crystallographic *c*-axis.

2) The observed deviation from *mmm* symmetry exhibits a systematic dependence on doping (Fig. 2 main text), which is unlikely to arise from random misalignment especially given that the identical alignment procedure is used for all samples.

3) A crystal with *mmm* point group symmetry only has three axes of two-fold rotational symmetry, namely the orthorhombic *a*-, *b*- and *c*-axes. Therefore if the optical axis of the experiment is not along one of these axes, the RA patterns will not exhibit two-fold rotational symmetry. The fact that we do observe two-fold rotational symmetry in the RA patterns (Fig. 2 main text) thus excludes the possibility that what we observe results simply from a small *c*-axis misalignment of an orthorhombic crystal.